2024

Development of a mechanistic chamber model for twin-screw compressors with detailed sub-models for estimating the bearing loads

Abhignan Saravana
saravan0@purdue.edu

Haotian Liu
liu1460@purdue.edu

Eckhard A. Groll
groll@purdue.edu

Davide Ziviani
dziviani@purdue.edu

Development of a mechanistic chamber model for twin-screw compressors with detailed sub-models for estimating the bearing loads

Abhignan SARAVANA[(1*)], Haotian LIU[(1)], Eckhard A. GROLL[(1)], Davide ZIVIANI[(1)]

[(1)] Ray W. Herrick Laboratories, School of Mechanical Engineering, Purdue University
West Lafayette, 47907-2099, USA
saravan0@purdue.edu; liu1460@purdue.edu; groll@purdue.edu; dziviani@purdue.edu

* Corresponding Author

ABSTRACT

For a detailed performance evaluation of oil-injected twin-screw compressors, it is of utmost importance to understand and model the advanced physical phenomena occurring during the compression process (e.g., mass and heat transfer mechanisms) as well as analyze the mechanical behavior of the compressor (e.g., rotordynamics, bearing loads, leakage flows). Upon establishing such a model, it is important to verify and validate the results using experimentally generated data or previously verified model.

This paper presents a method to perform a thorough numerical computation of the torque and bearing loads followed by bearing losses due to friction, on a 4/6 oil-injected twin-screw compressor with slide-valve part-load modulation and economization. Using data from a previously established experimental setup, this model has been verified and validated with the help of SCORG and PDSim. Indicated diagrams and mechanistic analyses were developed and have been analyzed to experimentally quantify the various losses and to validate the models. The validated model is used to analyze the performance of the compressor.

1. INTRODUCTION

Over the years, various types of twin-screw compressors have been designed and developed to optimize their operation. Research studies focused on both thermodynamic aspects (*e.g.,* volume ratio control, oil injection) and manufacturing (*e.g.,* profile generation, optimization of contact lines). The twin-screw compressor is a positive displacement machine rotary compressor with helical-like compression chambers. The male and female rotors are the main components of a twin-screw compressor and they function as both a compression mechanism and a gear pair. It follows that the profile generation is based on gearing theory, as described by Stosic et al. (2005).

The kinematics model of the meshing profiles is the first step to compute the cavity volumes of the working chambers that are necessary to develop detailed mechanistic models of twin-screw machines (Tang, 1994 and Koai 1990). Specifically, several comprehensive models are described in the literature with different levels of complexity. For this project, the thermodynamic aspects need to be linked with the estimation of the forces and moments acting on the rotors as well as on the bearings. At the Herrick Labs, Adams (1993) developed a computer model to study the interactions between the rotors and compute the backlash type rotor vibrations (chatter) as well as bearing forces. The forces and moments due to gas compression were computed using vector calculus principles to integrate the chamber pressure over the rotor surfaces. The 3-dimensional surface of each rotor was mapped to a 2-dimensional region. Koai (1990) also included the effect of a slide-valve capacity control mechanism. Additional studies that covered the analyses of forces and moments in twin-screw compressors were conducted by You (1994) and Tran et al. (2016). Seshaiah et al. (2019) performed a deeper analysis on thermodynamic performance parameters of twin screw air compressors such as efficiency, delivery rate and the heat of compression of the compressors. More recently, Saravana et al. (2022) developed a method to analyze experimentally obtained pressure volume curves and conduct performance analysis. Sun et al. (2021) developed a test rig to test variable speed, variable slide valve configuration twin screw compressors and conducted noise analysis and indicated power calculation with the help of indicator diagrams. Yang et al. also presents a CFD validation to experimentally obtained internal pressure characteristics (Yang 2021)

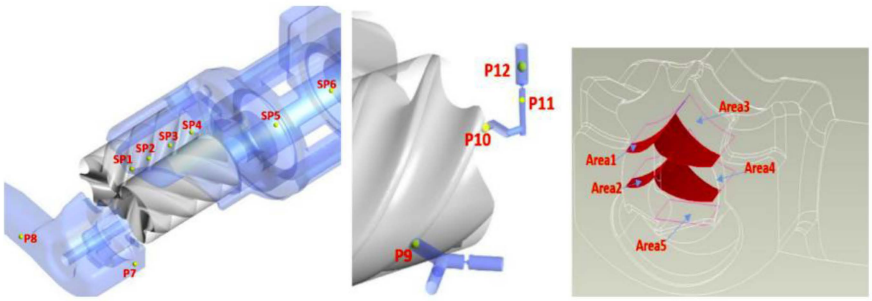

Figure 1: All the monitoring point locations in the fluid domains (Yang 2021)

In most of these studies, the models were validated by employing internal pressure sensors to reconstruct the indicated diagram of the compression process as well internal temperature measurements. With respect to bearing loads, Hou et al. (2017) conducted an experimental study on the axial force on the rotors of a twin-screw compressor operating at high pressures such those found in high temperature heat pumps or NH_3/CO_2 cascade refrigeration systems. Dynamic pressure sensors were employed to measure the in-chamber pressure traces, a piezoresistive force sensors were installed at the discharge end of the male rotor to characterize the loads on the rolling bearing. Janicki (2007) also presents a simulation model to predict performance parameters and model leakages for a 3-5 configuration twin-screw compressor

2. TWIN-SCREW SETUP

2.1 Test Matrix

The test matrix consisted of 26 operating conditions with a wide range of parameters, including suction and discharge pressure, volume ratio, load capacity dictated by the slide valves and slide stops as well as rotational speed. These parameters control the thermodynamic performance of the twin-screw compressor. More details on the operating conditions can be found in Appendix A.

Table 1: Test matrix for reference caseS

Test	RPM	P_{SUC} (psi)	P_{DIS} (psi)	Volume Ratio	Load	$\dot{m}_{suc}$ (lbm/min)	$\dot{m}_{dis}$ (lbm/min)
2	1800	25	175	4.1	100	175.803	178.747
0	1800	60	225	2	100	414.643	417.504

2.2 Open-Drive Twin-Screw Compressor Unit

An open-drive twin-screw compressor with a 4/6 rotor configuration model has been identified as the unit to be modelled and tested as part of this study. The main geometry parameters of the rotors are reported **Table 2**. Detailed information regarding the rotor profiles can be found in a previous study conducted by the authors (Salts et al., 2019).

Table 2: Screw rotor main geometric parameters.

Parameter	Value
Theoretical displacement	0.90402 ft^3/rev (25599 cm^3/rev)
Compressor volume ratio	2.0-4.1
Rotor wrap angle, φ_w	325°
Male rotor lead (right hand helix)	752 mm (29.6063 in)
Female rotor lead (left hand helix)	1128 mm (44.4094 in)
Male lobes, z_1	4
Female lobes, z_2	6
Center distance, $A_{O_1O_2}$	222 mm
Rotor length, L	679.20 mm
L/D_m	2.40

3. COMPRESSOR MODELING THEORY

3.1 Geometry Calculations and Rotor Grid Generation

Geometry calculations are necessary to understand the compression process within the screw compressor and compute the compression loads. As it can be seen in **Figure 2**, the rotor grid geometry consists of the profile rotated around the rotor cross section and revolved around the helix of the rotors using parameters such as the pitch and wrap angle. The cavity between the rotor lobes/grooves is filled in with a polygon clipping and this tracks the active compression chamber. These sections progress with compression angle and the area of the active compression chamber is integrated along the length of the rotor to form the volume curve in **Figure 5a)**. The port areas in **Figure 5b)** are obtained in a similar way, where the rotors are rotated until the compressed gas comes in contact by the suction and discharge ports. The port areas are then computed as an intersection between the active chamber and the shape of the ports. **Figure 5a)** also presents a validation between the numerical result and experimental. The curves overlap very well with the maximum volumes differing by only 1%. The angles might be shifted slightly, and this may be due to the offset angle in the experimental setup where there is a delay in the opening of the rotors threads to suction gas.

For a more detailed model, an unwrapped view was also generated to help analyze slide valve modulations with the volume ratios. The slide valve position is dictated by a relation between the slide valve distance and the volume ratios. This is shown in **Figure 3a)**. The dotted black line represents the suction and discharge radial ports, and the green section represents the slide valve overlapping the discharge radial port to reduce or increase discharge volume, thereby changing volume ratios. The unwrapped view is developed based on the idea that the 3D circumference of the rotor is unwrapped onto a 2D plane, and the rotors are distributed at various locations along this circumference. The box with the black outline represents the active chamber and the unwrapped compression chamber progresses through this with change in crank angle of rotation.

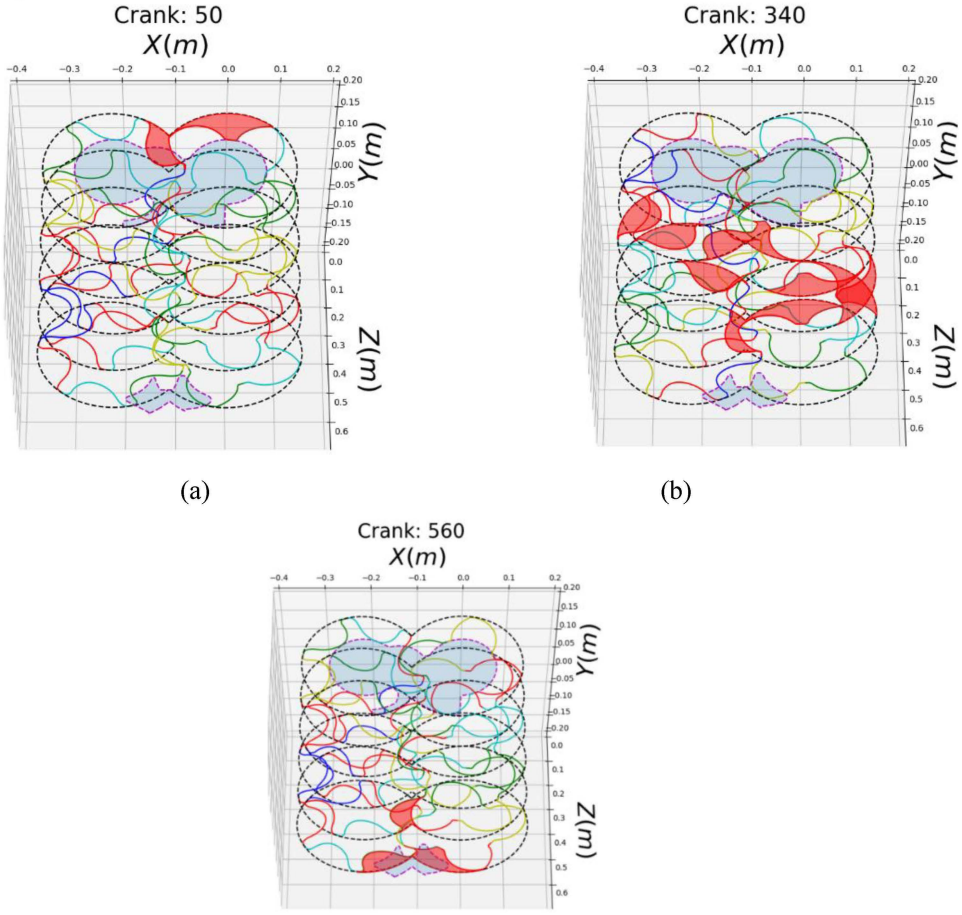

(a) (b)

(c)

Figure 2: Progression of compression chamber from a) Suction to b) Suction close (maximum volume) c) Discharge.

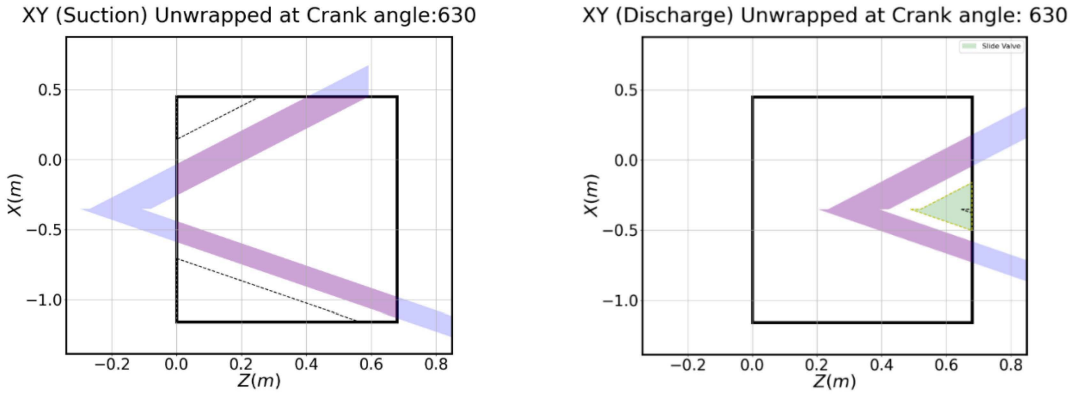

(a) (b)

Figure 3: Unwrapped views for a) Suction radial port b) Discharge radial port

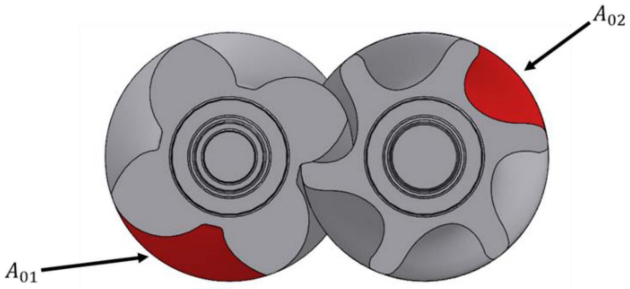

Figure 4: Cavity areas of male and female (suction end view)

3.2 Volume Curves and Porting

The rotor geometry consists of a two-dimensional rotor profile, the rotor length, and the rotor wrap angle. As the male rotor rotates, the working chamber boundaries are the interfaces between the rotors and the suction and discharge planes, the rotor lobe tip and housing interfaces, and the interlobe seal curve between the male and female rotors. These boundaries define the limits of integration for each chamber in order to obtain the chamber volume and its surface. At a certain male rotor angle, the cavity area of a working chamber is bounded by a set of curves that can be expressed in the parametric form:

$$\begin{cases} x_i = x_i(t_i) \\ y_i = y_i(t_i) \end{cases} \tag{1}$$

where t_i is the running parameters for each curve. The set of curves can also be defined by a discrete set of data points. The cavity area (cross-section area) can be obtained by utilizing principles of polygon calculations:

$$A_z(\theta_1) = \frac{1}{2}\oint x dy - y dx \cong \frac{1}{2}\sum_i \int_{t_{\mathrm{i,min}}}^{t_{\mathrm{i,max}}} (x_i y_i' - y_i x_i')\, dt_i \tag{2}$$

The male and female maximum cavity areas are shown in **Figure 4**. Once the cavity areas are evaluated, the volume of the chamber at a rotation angle θ_1 is given by:

$$V(\theta_1) = \sum A_z(\theta_1)\, \Delta z = \sum A_z(\theta_1) \frac{L_{rotor}}{\varphi_w} \Delta\tau_1 \tag{3}$$

where τ_1 is the twist parameter of the male rotor. For completeness, two additional methods can be potentially employed to determine the cavity volume in twin-screw compressors (Zaytsev, 2003) which are not considered in the current modeling effort:

i. method based on the analytic relation between the volume and its boundary surface;

ii. method based on the principle of virtual work

By knowing the cavity areas, as the rotation of the male rotor advances, polygon operations can be applied to determine the overlapping area with the suction and discharge ports. The cavity volume curve and the suction and discharge port areas as a function of male rotor rotation are shown in **Figure 5**. The total rotation angle that characterizes a complete volume curve is defined as:

$$\theta_{1,max} = 2\pi + \varphi_w + \frac{2\pi}{z_1} + \cos^{-1}\left(\frac{A_{O_1O_2}^2 + r_{o1}^2 - r_{p2}^2}{2A_{O_1O_2}r_{o1}}\right) \quad (4)$$

where r_{o1} is the outer radius of the male rotor.

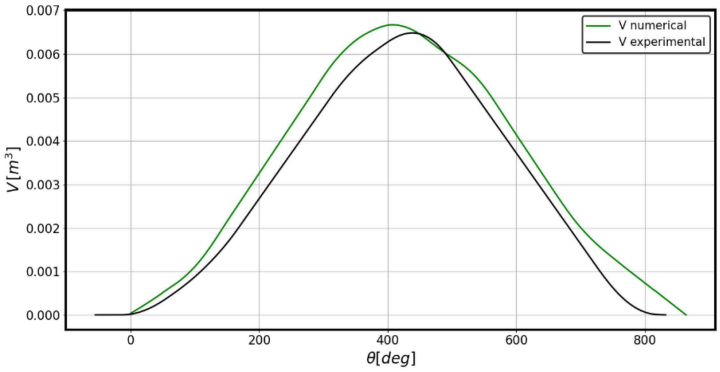

(a)

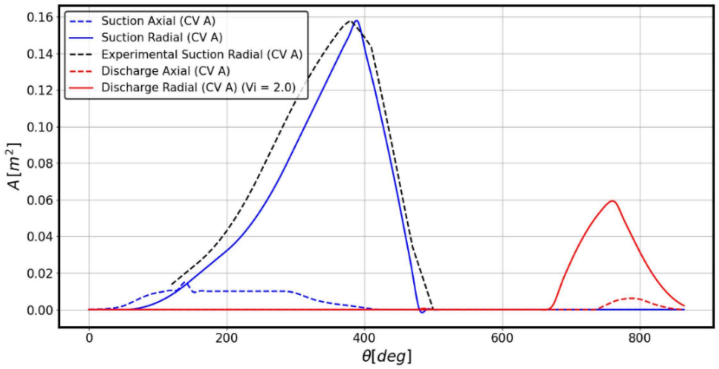

(b)

Figure 5: a) Cavity volume curve and b) suction and discharge port areas.

3.3 Sealing Lines and Area Curves

The forces acting on the rotors are mainly due to gas compression loads that act normally to the surface of the rotors (the weight of the rotors is considered as well when balancing the forces). However, the surface of the rotors under pressure load is constrained by the lobe tip sealing curves or the inter-lobe sealing curves depending on the stage and angle of rotation, as illustrated in **Figure 6**. The pressure loads that act normal to the sealing boundary formed between the lobe tips and inter-lobe contact of male and female rotors are decomposed into radial and axial components. Therefore, for accurate force analysis, it is important to describe the sealing lines and areas engaged.

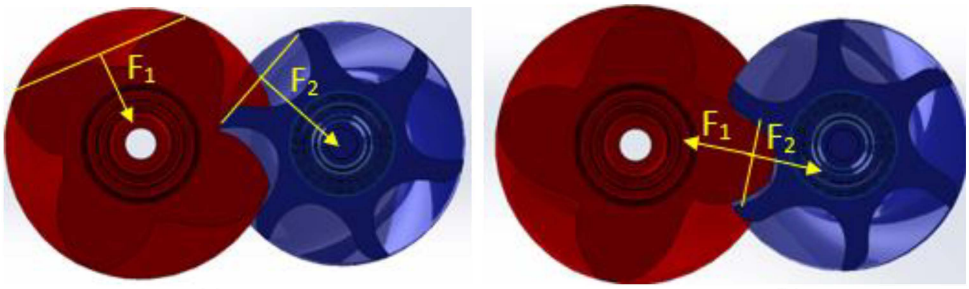

(a) (b)

Figure 6: Simplified schematic of pressure loads acting normal to the a) lobe tips and b) inter-lobe seal line (reproduced from (Adams, 1997))

One way to accomplish this is by studying the rotor profile more closely. The 3D rotor lobes area was created using the phase shifted versions of the same rotor profile for each lobe. If the rotor profiles are rotated along the helix using a certain pitch and wrap angle, the entire rotor grid can be generated. This method was used to generate the 2D sealing lines for one lobe as illustrated in **Figure 7** and followed the method described by Tran et al. (2016). By using simple projections, the 3D sealing lines can be projected onto two planes: XZ and YZ as illustrated in **Figure 8**. These curves are enclosed within an active compression chamber and the entire 2D compression chamber will translate with crank angle, thus only engaging a portion of the compression chamber under gas compression at a time. Using polygon clipping techniques, several force related quantities such as areas, area moment, centroid and perimeter can be computed. One such example of area curves for the male rotor is displayed in **Figure 9**.

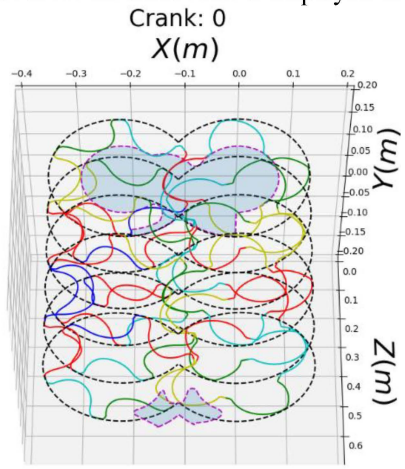

Figure 7: 3D rotor reconstruction with axial suction and discharge ports

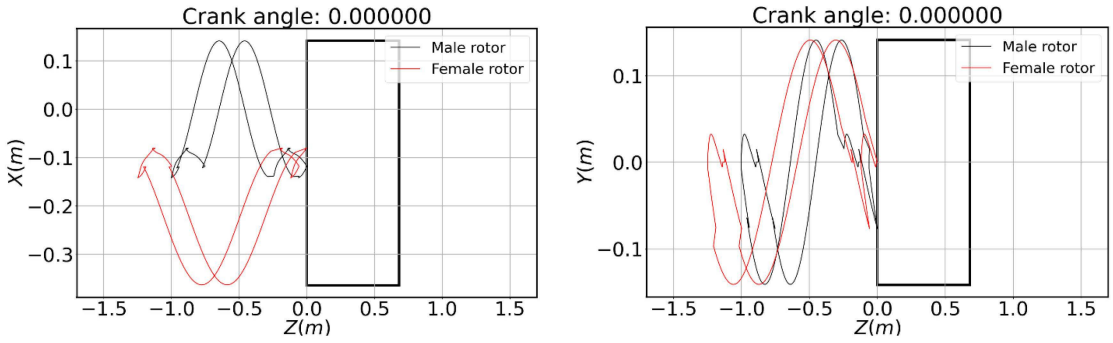

(a) (b)

Figure 8: 2D projections of sealing lines on (a) YZ plane (b) XZ plane.

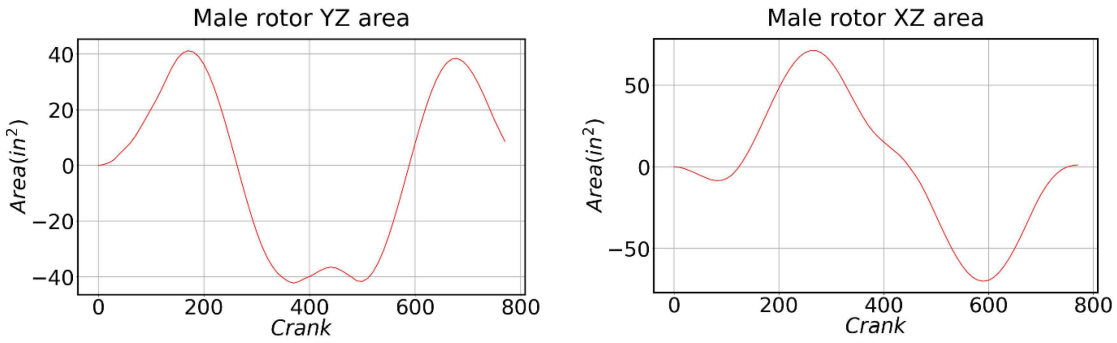

(a) (b)

Figure 9: 2D projections of sealing lines on (a) YZ plane (b) XZ plane

3.4 Three-dimensional Mechanistic Force Analysis

The surface area projections on X-Z and Y-Z between the sealing line boundary are used to compute area moment of inertia which are then used to compute torque, axial, and radial forces. The gas compression force balance on the rotors is illustrated in **Figure 10** while the bearing load force balance is displayed in **Figure 11**. Equations 5-7 summarize a numerical method for resolving pressure loads while Equations 8-11 describe the computation of bearing loads based on the resolved gas pressure loads. A general moment and force balance can be used to compute the forces acting on the rotor assembly using the following assumptions:

- Z axis has been chosen as the rotation axis in the axial direction whereas X and Y axis represent radial planes.
- Axial and radial force contributions are to be balanced by the pressure forces and suction and discharge bearings.
- Mass of the rotors is not indicated in **Figure 10** and **Figure 11** for simplicity. However, the mass is included in the moment balance equations.
- The pressure load acts uniformly throughout the working chamber (male and female) for every crank angle rotation. Sp

$$F_{1Z}(i) = P\left(\frac{(x_A+x_B)(x_B-x_A)}{} + \frac{(y_A+y_B)(}{}\right.$$

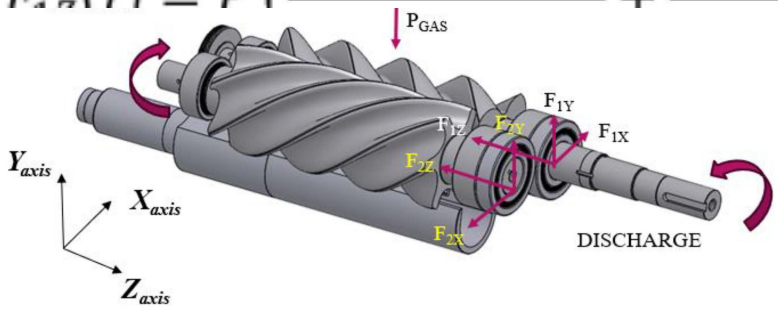

Figure 10: Mechanistic Force Diagram for resolving pressure loads (radial, axial and torque)

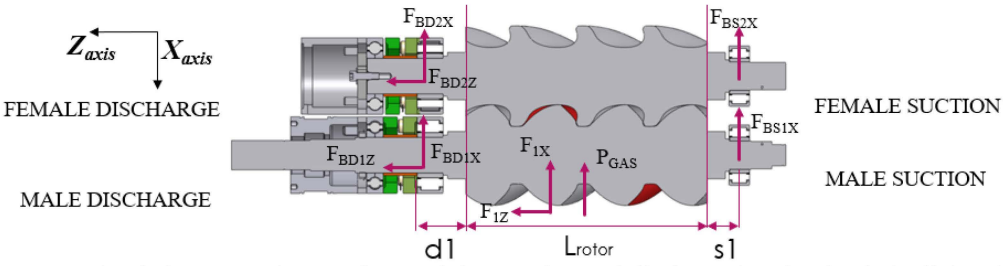

Figure 11: Mechanistic Force Diagram for resolving suction and discharge bearing loads (radial and axial).

$$F_{1Z}(i) = \frac{2\pi}{L_d}.T_1 = \frac{2\pi}{L_d}.\int_A^B x.F_Y + y.F_x \tag{5a}$$

$$F_{1Z}(i) = P\left(\frac{(x_A+x_B)(x_B-x_A)}{2} + \frac{(y_A+y_B)(y_B-y_A)}{2}\right)z_{AB} \tag{5b}$$

$$F_{1Z}(i) = P.\left(x(i_c).(area\ XZ) + y(i_c).(area\ YZ)\right) \quad (5c)$$

$$F_{1X}(i) = \int_A^B P dy dz = P(y_B - y_A) z_{AB} \quad (6)$$

$$F_{1y}(i) = \int_A^B P dx dz = P(x_B - x_A) z_{AB} \quad (7)$$

$$\sum M_y = \left(d_1 + z(i_c)\right).F_{1X}(i) - x(i_c) * F_{1Z}(i) + \ (s_1 + L_{rotor} + d_1).F_{BS1X}(i) = 0 \quad (8)$$

$$\sum F_y = F_{1Y}(i) + F_{BD1Y}(i) + \ F_{BS1Y}(i) = 0 \quad (9)$$

$$\sum M_x = -\left(d_1 + z(i_c)\right).F_{1Y}(i) + y(i_c).F_{1Z}(i) - \ (s_1 + L_{rotor} + d_1).F_{BS1Y}(i) = 0 \quad (10)$$

$$\sum F_x = F_{1X}(i) + F_{BD1X}(i) + \ F_{BS1X}(i) = 0 \quad (11)$$

where i: each profile point along the length of the rotor and in between two rotor lobe tips; B: bearing; L_{rotor}: rotor length; T: torque; L_d: helix lead; P: Pressure. Surface integration limits A and B are profile points at the leading and lagging rotor lobes (different from bearing subscript 'B'). Here F_{BS1X}, F_{BD1X}, F_{BS1Y}, F_{BD1Y} represent suction and discharge bearing loads in X and Y radial directions respectively and are the unknowns to be computed from the above equations.

Having computed the radial forces, torque is a byproduct of the moment balance around the rotational Z axis as shown in Equation 12. This numerically obtained torque power (product of numerical torque and rotational speed) can be compared with the experimental torque power or shaft power and the mechanical losses can be obtained (Equation 13-15). Employing a modest frictional factor, the oil drag, and frictional losses of the bearings are obtained as well.

$$T = \int_A^B x.F_Y + y.F_x = \int_A^B \left[x.Pdx \int_0^z dz + y.Pdy \int_0^z [\![dz]\!]\right] \quad (12a)$$

$$T = P.\left(x(i_c).(area\ XZ) + y(i_c).(area\ YZ)\right) \quad (12b)$$

$$\dot{\bar{T}}_{rotor} = \left(T_1 + \frac{z_1}{z_2} T_2\right)/360 \quad (13)$$

$$\dot{\bar{W}}_{compr} = \frac{2\pi N_1}{60}\left(\dot{\bar{T}}_{rotor}\right) \quad (14)$$

$$\dot{\bar{W}}_{losses} = \dot{\bar{W}}_{shaft} - \dot{\bar{W}}_{compr} \quad (15)$$

where T represents torque on the rotor; $\dot{\bar{W}}_{compr}$, $\dot{\bar{W}}_{shaft}$, $\dot{\bar{W}}_{losses}$ represents cycle-averaged overall compression power, overall shaft power and overall power losses respectively; N represents rotational speed; z represents number of rotor teeth and the subscripts 1 and 2 pertain to male and female rotor abbreviations, respectively.

4. TORQUE AND FORCE VALIDATION

The numerical results obtained using the equations above were compared with the experimental results for one example case and they are used to validate the mechanistic model. **Figure 12**, **Figure 13**, **Figure 14** display preliminary axial, radial, and torque loads. The torque, radial load plots agree well with experimental results while some discrepancy can be seen on the male axial force data. This can be attributed to the missing pressure loads acting on the axial end faces which are not considered in this part of the model. The end face force estimations can be added onto the numerical results produced. The average end face forces can be estimated using the following equation with an example already calculated for test #2 (Hou et al.,2017).

$$F_{eav} = \frac{1}{4}(P_{dis} - P_{suc})\left(A_{male} - A_{journal}\right)$$

$$= 0.25 * (1206.59 - 172.37)kPa * (0.02905 - 0.0065)m$$

$$= 5.83kN * 224.81\frac{lbf}{kN} = 1310.6\ lb - ft \quad (16)$$

Similar results can be observed in **Figure 15** and **Figure 16**, although the model predicts a much lower torque result than the experimental conditions.

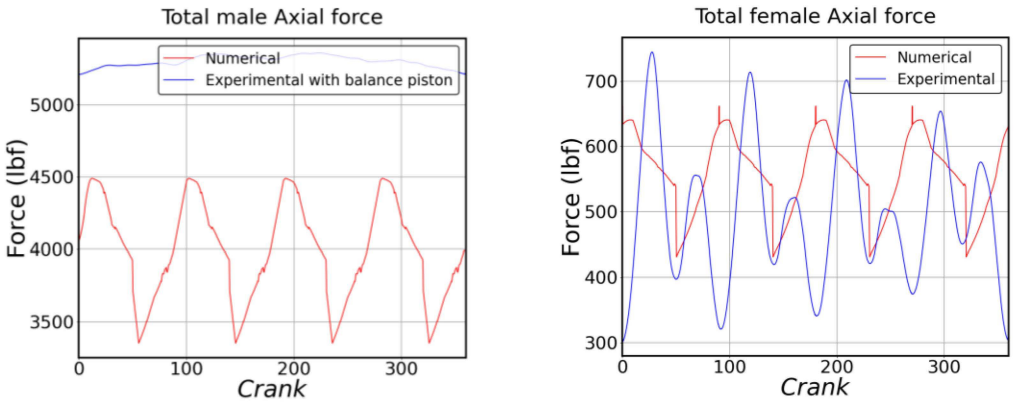

(a) (b)

Figure 12: Axial force comparison between experimental and numerical results for (a) Male rotor (b) Female rotor (test #2). Rotor end face forces are not included in these plots.

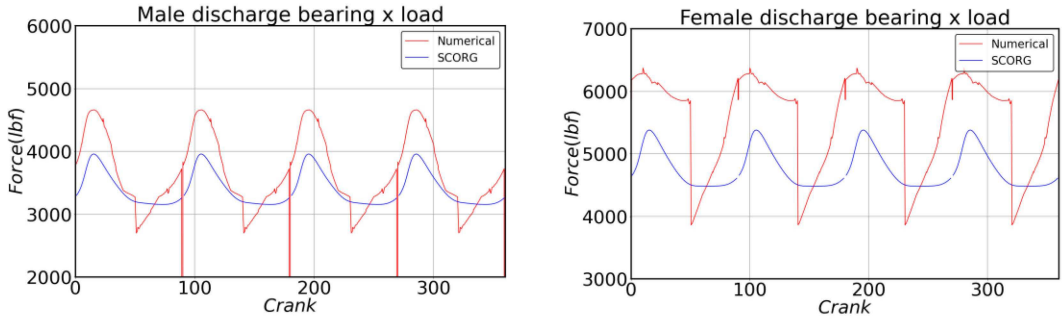

(a) (b)

Figure 13: Discharge bearing load in X axis comparison between SCORG (PDM Analysis, 2022) and numerical results for (a) Male rotor (b) Female rotor.

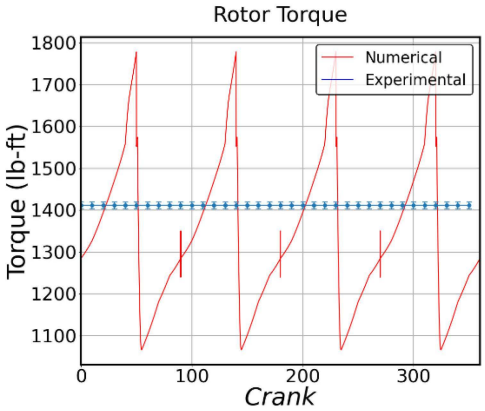

Figure 14: Total male rotor torque load comparison between numerical and experimental result (test #2). The experimental torque was obtained with a torque meter.

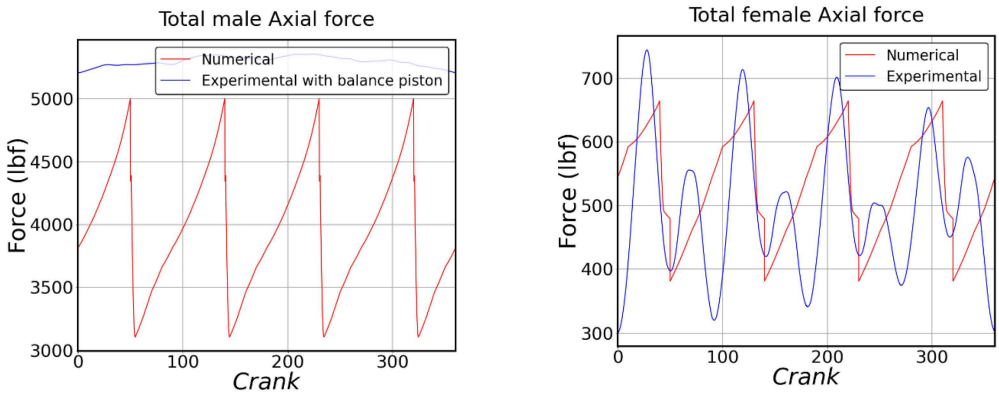

(a) (b)

Figure 15: Axial force comparison between experimental and numerical results for (a) Male rotor (b) Female rotor (test #0). Rotor end face forces are not included in these plots.

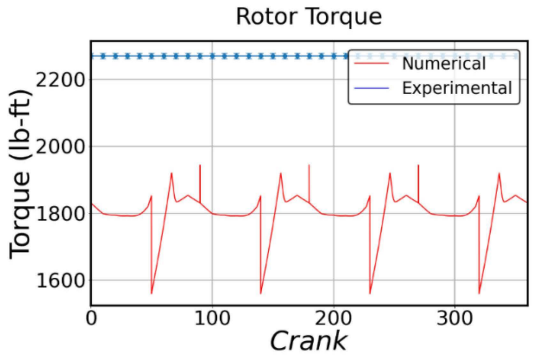

Figure 16: Total male rotor torque load comparison between numerical and experimental result (test #0). The experimental torque was obtained with a torque meter.

6. CONCLUSION AND FUTURE WORK

In this project, a comprehensive screw compressor model has been developed to estimate bearing loads, forces and moments on the rotors. The model is able to capture the physics of the compression process and estimates the forces and moments using a thorough mechanistic force balance which is validated with experimental results.

A screw compressor was fully instrumented with high-frequency pressure transducers to reconstruct the indicated diagram under various operating conditions. A methodology has been developed to align the pressure signals and process the transient results to get working cycle averaged indicated diagrams and compute indicated power, indicated losses, and estimate the mechanical losses. The experimental results have been used to carry out a thorough validation.

Within the model, there are a few areas of improvements that can be pursued to increase the accuracy of the model:

- Addition of end face axial forces
- Improvement of friction models to better estimate frictional losses and accurately estimate mechanical efficiency

NOMENCLATURE

A	Area	ft^2
θ	crank angle	deg
d	discharge bearing offset	$in\ (or\ m)$
F	Force	N (or lbf)
W_{ind}	indicated work	$lb-ft$
L_{d1}	male rotor lead	ft
L_{rotor}	rotor length	ft
W_{loss}	loss in work	$lb-ft$
M	Moment	N-m (or lbf-ft)
z_1	number of male rotor lobes	$-$
r_p	pitch circle radius	$lbf-\frac{ft}{lbm-Rankine}$
$\dot{W}$	power	hp
P	pressure	$psia$
φ_w	wrap angle	deg
s	suction bearing offset	$in\ (or\ m)$
t	time	min
T	Torque	N-m (or lbf-ft)
V	Volume	ft^3

Subscript

comp	compressor	mech	mechanical
dis	discharge	pos	position
exp	experimental	shaft	shaft
isen	isentropic	suc	suction
ind	indicated	z	In the z axis
max	maximum	pos	position
Male rotor	1	Vol	Volumetric
X	In the x axis	Female rotor	2
eav	End face average force	y	In the y axis

REFERENCES

Adams, G.P., "Modelling and computer simulation of rotor chatter and oscillating bearing forces in twin screw compressors", PhD Thesis, Purdue University, 1993.

Hou F., Zhao Z., Yu Z., Xing Z. (2017). Experimental study of the axial force on the rotors in a twin-screw refrigeration compressor. International Journal of refrigeration, 75, 155-163. DOI:http://dx.doi.org/10.1016/j.ijrefrig.2017.01.002

Janicki, M. (2007). Modellierung und simulation von Rotationsverdrängermaschinen von Magnus Janicki.

Koai, K-L, "Mathematical modeling of twin screw compressors with special attention to gas pulsations in three-dimensional gas paths", PhD Thesis, Purdue University, 1990.

PDM Analysis, (2022). SCORG. Link: https://pdmanalysis.co.uk/scorg/

Salts, N., Ziviani, D., & Groll, E. A. (2019). Application of a generalized compressor modeling framework for simulating an oil-injected twin-screw compressor. IOP Conference Series: Materials Science and Engineering, 604(1), 012009. https://doi.org/10.1088/1757-899x/604/1/012009

Saravana, A., Liu, H., Groll, E. A., & Ziviani, D. (2022). Experimental and numerical analyses of the thermodynamic and mechanical performance of an oil-injected and economized 4/6 twin-screw compressor. IOP Conference Series: Materials Science and Engineering, 1267(1), 012022. https://doi.org/10.1088/1757-899x/1267/1/012022

Seshaiah, N., Sahoo, R. K., & Sarangi, S. K. (2010). Theoretical and experimental studies on oil injected twin-screw air compressor when compressing different light and heavy gases. Applied Thermal Engineering, 30(4), 327–339. https://doi.org/10.1016/j.applthermaleng.2009.09.010

Stosic, N., Smith, I., Kovacevic, A., "Screw Compressors – Mathematical Modelling and Performance Calculations". Springer, 2005

Stosic N, Milutinovic L, Hanjalic K, et al. (1990). Experimental investigation of the influence of oil injection upon the screw compressor working process. In International compressor engineering conference, Purdue University, West Lafayette, Indiana, USA, 17–20 July 1990 (pp.34–43)

Sun, S., Xing, Z., Li, Y., Su, P. C., & Chen, W. (2021). Experimental investigation on twin screw refrigeration compressor with different capacity control methods. International Journal of Refrigeration, 130, 370–381. https://doi.org/10.1016/j.ijrefrig.2021.04.020

Tang, Y., "Computer aided design of twin screw compressors", PhD Thesis, University of Strathclyde, Glasgow, UK, 1994.

Wu, Y. R. and Tran, V. T. (2016). Dynamic response prediction of a twin-screw compressor with gas-induced cyclic loads based on multi-body dynamics. International Journal of Refrigeration, 65, 111–128. https://doi.org/10.1016/j.ijrefrig.2015.12.002

Yang, S., Ouyang, H., Wu, Y., Wang, L., Mei, L., & Wang, H. (2021). CFD simulation for the internal pressure characteristics of an oil-injected twin-screw refrigeration compressor. International Journal of Refrigeration, 126, 143–154. https://doi.org/10.1016/j.ijrefrig.2021.01.020

You, C.X., "A theoretical study of rotor forces and torques in helical twin screw compressors", PhD Thesis, University of Strathclyde, Glasgow, UK, 1994.

Zaytsev, D. V. (2003). (thesis). Development of wet compressor for application in compression-resorption heat pumps. s.n., S.l.

ACKNOWLEDGEMENT

The authors would like to thank Johnson Controls International for sponsoring this research project.

APPENDIX A

Table A1a: Test matrix

Test	1-	3	4	5	6	7	8	9
RPM	1800	3600	3600	3600	3600	3600	3600	3600
P_{SUC} (psi)	60	25	25	25	25	40	40	40
P_{DIS} (psi)	225	175	175	175	175	125	125	125
Volume Ratio	2	2	3	4.1	4	2.3	3.5	2
Load	75	100	100	100	100	100	100	100
$\dot{m}_{suc}$ (lbm/min)	293.149	355.52	364.211	364.782	366.27	589.737	587.59	586.796
$\dot{m}_{dis}$ (lbm/min)	296.164	359.87	368.413	368.646	370.19	591.434	587.839	588.376

Table A1b: Test matrix (continued)

Test	10	11	12	13	14	15	16	17
RPM	3600	3600	3600	1800	1800	1800	1800	1800
P_{SUC} (psi)	40	40	25	40	40	40	40	40
P_{DIS} (psi)	125	125	175	125	125	125	125	125
Volume Ratio	3	4.1	3.5	2	3	3.5	4.1	2.3
Load	100	100	100	100	100	100	100	50
$\dot{m}_{suc}$ (lbm/min)	590.606	582.096	364.519	288.62	291.967	288.547	284.428	157.271
$\dot{m}_{dis}$ (lbm/min)	591.666	583.587	368.518	290.977	294.289	290.949	286.57	159.926

Table A1c: Test matrix (continued)

Test	18	19	20	21	22	23	24	25	26
RPM	1800	1800	1800	1800	1800	1800	1800	1800	1800
P_{SUC} (psi)	40	40	40	40	40	60	60	60	60
P_{DIS} (psi)	125	175	225	225	225	175	175	175	175
Volume Ratio	2.3	2.7	2	2.3	4.1	2	3.1	4.1	2.5
Load	75	100	100	100	100	100	100	100	100
$\dot{m}_{suc}$ (lbm/min)	194.928	280.035	266.646	272.977	275.999	420.747	421.28	412.292	428.081
$\dot{m}_{dis}$ (lbm/min)	197.482	283.653	270.095	276.819	279.003	426.172	424.385	419.349	431.331